Int. J. Heat Mass Transfer. Vol. 37, No. 2, pp. 293–302, 1994
Printed in Great Britain

0017–9310/94 $6.00 + 0.00

Measurement and interpretation of growth and evaporation of monodispersed droplets in a shock tube

F. PETERS† and B. PAIKERT‡

† Universität Essen Schützenbahn 70, 45127 Essen, Germany
‡ ASEA Brown Boveri, CH 5405 Baden, Switzerland

(*Received* 2 *December* 1992 *and in final form* 6 *May* 1993)

Abstract—A special gasdynamic shock tube process in combination with a Mie light scattering method is used to study growth and subsequent evaporation of monodispersed droplets carried in argon or air. The droplets are generated by homogeneous nucleation and observed in the μm range (0.15–6 μm radius). Droplet concentrations range from 10–1000 mm^{-3}. Four different substances, i.e. water, *n*-propanol, methanol and *n*-hexane are tested for a wide range of properties. A model covering the entire range between large ($Kn \gg 1$) and small Knudsen numbers ($Kn \ll 1$) is applied to interpret the experimental data. Excellent agreement is found.

1. INTRODUCTION

DROPLETS suspended in a carrier gas/vapor mixture grow or evaporate according to the state of the vapor. If the vapor is supersaturated it diffuses through the carrier towards the droplet and condenses on its surface. At the same time the latent heat of condensation is conducted away from the droplet. If the vapor is undersaturated the reversed process takes place. Both processes aim for equilibrium.

The objective of this work is to measure droplet radius vs time during condensation and evaporation for various substances and thermodynamic states. Homogeneous nucleation, studied previously by the authors [1], is presently utilized for droplet generation. The droplets growing from nuclei are monodispersed, not interactive, evenly distributed in space and at rest relative to the carrier. This is certainly an ideal system hardly representing real sprays. On the other hand any detailed understanding of real sprays requires the knowledge of the behavior of simpler ones. And even for such simple systems experimental work is scarce. The following work overlaps to some extent with what we have done.

A number of investigations on the growth of water droplets in various carriers were conducted by Vietti and Fastook [2]. They employed an expansion chamber with a Mie light scattering technique providing radius vs time results although the droplet size distribution was quite substantial. They found no consistent way of matching their extensive results with theoretical models. For a review of this work Wagner [3] may be consulted.

Wagner himself [3, 4] developed a fast expansion chamber with a sophisticated multi-angle scattering technique. Using latex aerosols as condensation sites quite monodispersed water droplets could be grown. Supersaturations were up to 3.5, much above the level of atmospheric cloud chambers. The results supported successfully a theoretical model with accommodation coefficients of unity.

More expansion chamber experiments with optical detection of water droplets grown on NaCl aerosols were described by Hagen *et al.* [5]. They confirmed condensation coefficients of unity only for 'fresh drops'. Aged drops grew slower.

Evaporation of DOP droplets behind shock waves in argon was studied by Roth and Fischer [6] in a shock tube. They evaluated radius vs time results using a light scattering system. By applying model calculations to the results they determined transitional correction factors and compared those with literature values.

Another shock tube study was carried out by Goosens *et al.* [7] who made use of light extinction to measure the evaporation times of water droplets in nitrogen after passage of a shock wave. The water droplets were heterogeneously condensed onto solid aerosols. Agreement with a simple model was found.

2. MODEL PREPARATION

We consider monodispersed droplets evenly distributed in the carrier/vapor mixture. They are at rest with respect to the carrier. This is exactly the situation realized in our experiment. The spacing between droplets is sufficiently large to neglect direct interaction. Sedimentation is supposed not to occur on the time scale of the experiment. Under these circumstances the treatment of an individual droplet stands for all droplets. The gas volume assigned to each droplet equals the inverse droplet number concentration.

The heat and mass transfer between droplet and

NOMENCLATURE

c_p	isobaric specific heat capacity
D	diffusion coefficient
J	nucleation rate
J_m, J_q	mass and conduction heat flux density
k_B	Boltzmann constant
k	thermal conductivity
Kn	Knudsen number, $\lambda/2r_d$
L	latent heat
m	molecular mass
n	refractive index
N	number of molecules; number density in equation (16)
p	pressure
p_e	equilibrium vapor pressure
Pr	Prandtl number of vapor/gas mixture
r_d	droplet radius
r_{im}, r_{iq}	radius of Knudsen-continuum interface for mass and heat transfer
R	specific gas constant
S	saturation ratio, i.e. vapor pressure over equilibrium vapor pressure
Sc	Schmidt number of vapor/gas mixture
T	temperature
v	molecular volume
V	volume.

Greek symbols

α	condensation and evaporation coefficient
γ	ratio of specific heat capacities
η	dynamic viscosity of vapor/gas mixture
λ	mean free path of vapor/gas mixture
ρ	density
σ	surface tension of liquid.

Subscripts

d	droplet
e	equilibrium
g	gas
i	Knudsen continuum interface
l	liquid
v	vapor
∞	ambient conditions far from droplet.

surroundings requires the solution of the transfer equations in the molecular, the continuous and the transition regime. For the continuous regime Fourier's heat transfer law and Fick's diffusion law apply in spherical coordinates. In the molecular regime the Hertz/Knudsen model based on the molecular impingement rate is frequently used. The decisive problem is the modelling of the transition region with Knudsen numbers close to unity.

There is a lot of theoretical work (e.g. Gyarmathy [8], Wagner [3], Mozurkewich [9], Barrett and Clement [10]) which may be consulted. We refer to a recent paper by Young [11]. Young provides a revised version of the Langmuir model matching the continuum fluxes with the molecular fluxes in the thin Knudsen layer about the droplet. The thickness of this layer is of the order of the mean free path. His final set of equations is suitable for practical calculations and comparisons with experimental results. Yet, we have to tailor these equations to our experimental circumstances which allow the following assumptions and approximations.

The transfer problem is spherical with the droplet of radius r_d in the center of the coordinate system. The gas/vapor volume alloted to each droplet is finite. Each volume is an adiabatic system of constant mass. It is much larger than the droplet with its thermal and diffusion boundary layers. This allows application of steady state equations with gradually changing boundary conditions (temperature T_∞ and vapor pressure $p_{v\infty}$).

The droplet temperature T_d is uniform throughout the droplet, i.e. surface temperature equals droplet temperature. The vapor pressure p_e at the surface is the equilibrium vapor pressure corresponding to T_d.

The deviation from equilibrium is small. That means small temperature and vapor pressure differences between droplet surface and 'infinity'. The temperature dependent property values should be evaluated at a mean temperature. Since the temperature span is small we evaluate at T_∞ which is known before T_d is computed.

The total pressure about a resting droplet is uniform. Thus pressure diffusion does not take place.

Thermal diffusion is neglected compared with Fick's diffusion.

The mass and thermal accommodation coefficients are set equal.

These assumptions are compatible with Young's analysis. His equations for the mass flux density in the continuous and the Knudsen layer regime, respectively, rewrite

$$J_m = \frac{r_{im}}{r_d}\sqrt{\left(\frac{R}{R_v}\right)}\frac{4Knp}{Sc\,p_{g\infty}}\frac{p_{vi}-p_{v\infty}}{\sqrt{(2\pi R_v T_\infty)}} \tag{1}$$

$$J_m = \frac{p_e\sqrt{\left(\frac{T_\infty}{T_d}\right)}-p_{vi}\sqrt{\left(\frac{T_\infty}{T_i}\right)}}{\sqrt{(2\pi R_v T_\infty)}\left(\frac{1}{\alpha}-\frac{r_d^2}{2r_{im}^2}\right)}. \tag{2}$$

The subscript i indicates the edge of the Knudsen layer. Since small temperature differences are assumed the ratios T_∞/T_d and T_∞/T_i are of order unity. Then p_{vi} can be eliminated from equations (1) and (2) to get

$$J_m = \frac{D(p_e - p_{v\infty})p}{R_v T_\infty p_{g\infty} r_d \left(\frac{r_d}{r_{im}} + \sqrt{\left(\frac{R}{R_v}\right)\frac{4Knp}{Sc\,p_{g\infty}}\left(\frac{1}{\alpha} - \frac{r_d^2}{2r_{im}^2}\right)}\right)}. \quad (3)$$

This involves the following definitions for the mean free path, the Knudsen and the Schmidt number

$$\lambda = \frac{16}{5}\sqrt{\left(\frac{RT_\infty}{2\pi}\right)}\frac{\eta}{p}; \quad Kn = \frac{\lambda}{2r_d}; \quad Sc = \frac{\eta}{\rho D}. \quad (4)$$

Young's equations for the heat flux in the continuous and the Knudsen layer regime, respectively, rewrite

$$J_q = \frac{r_{iq}}{r_d}\frac{k}{r_d}(T_i - T_\infty) \quad (5)$$

$$J_q = \frac{\frac{\gamma_v+1}{\gamma_v-1}\frac{p_{vi}R_v}{\sqrt{(2\pi R_v T_i)}} + \frac{\gamma_g+1}{\gamma_g-1}\frac{p_{gi}R_g}{\sqrt{(2\pi R_g T_i)}}}{\left(2 - \frac{r_d^2}{r_{iq}^2}\right)}(T_d - T_i). \quad (6)$$

Note that the definition of J_q has been changed by the factor $R_v T_\infty$. Furthermore we have omitted the last term of his equation (59) because it is numerically insignificant. We use the Prandtl number in the form

$$Pr = \frac{\gamma R\eta}{(\gamma-1)k} \quad (7)$$

and eliminate T_i, appearing in the parentheses, from equations (5) and (6) to get

$$J_q = \frac{k(T_d - T_\infty)}{r_d\left(\frac{r_d}{r_{iq}} + \frac{8Kn\gamma}{(\gamma-1)\Gamma Pr}\left(1 - \frac{r_d^2}{2r_{iq}^2}\right)\right)} \quad (8)$$

where

$$\Gamma = \sqrt{\left(\frac{T_\infty}{T_i}\right)}\left(\frac{\gamma_v+1}{\gamma_v-1}\sqrt{\left(\frac{R_v}{R}\right)}\frac{p_{vi}}{p} + \frac{\gamma_g+1}{\gamma_g-1}\sqrt{\left(\frac{R_g}{R}\right)}\frac{p_{gi}}{p}\right). \quad (9)$$

Again the temperature ratio T_∞/T_i is of order unity. The pressure ratios can be written, e.g. for the first one, $p_{vi}/p = (p_{v\infty}/p)(p_{vi}/p_{v\infty})$. Since the latter factor is of order unity we have

$$\Gamma \approx \left(\frac{\gamma_v+1}{\gamma_v-1}\sqrt{\left(\frac{R_v}{R}\right)}\frac{p_{v\infty}}{p} + \frac{\gamma_g+1}{\gamma_g-1}\sqrt{\left(\frac{R_g}{R}\right)}\frac{p_{g\infty}}{p}\right). \quad (10)$$

So far we have eliminated p_{vi} and T_i where they appear in differences and have approximated them where they appear as factors. It remains to assess the ratios r_i/r_d because they are not known. The difference $r_i - r_d$ is of the order of the mean free path. Therefore $r_i/r_d \to 1$ for $Kn \to 0$ and $r_i/r_d \to 0$ for $Kn \to \infty$. For our calculations we have also used these limits in the transition regime such that the first ratio in the denominator of equations (3) and (8) is set unity whereas the second is set zero. Thus

$$J_m = \frac{D(p_e - p_{v\infty})p}{R_v T_\infty p_{g\infty} r_d\left(1 + \sqrt{\left(\frac{R}{R_v}\right)\frac{4Knp}{\alpha Sc\,p_{g\infty}}}\right)} \quad (11)$$

$$J_q = \frac{k(T_d - T_\infty)}{r_d\left(1 + \frac{8Kn\gamma}{(\gamma-1)\Gamma Pr}\right)}. \quad (12)$$

For given ambient conditions the remaining unknowns of these equations are T_d, J_m and J_q. The missing equation is the relationship between the two fluxes and the latent heat

$$J_q = -LJ_m. \quad (13)$$

The droplet radius is calculated from the equation of continuity

$$\frac{dr_d}{dt} = -\frac{J_m}{\rho_l}. \quad (14)$$

3. EXPERIMENTAL METHOD

3.1. *The gasdynamic process*

As mentioned before we utilize homogeneous nucleation to generate monodispersed droplets in a carrier gas. In this work we neglect all nucleation aspects except those needed to understand the generation mechanism.

The vapor–liquid phase transition in the absence of foreign surfaces takes place by dropwise condensation in the supersaturated state of the vapor. The droplets emerge from nuclei born at the critical size r^*, given by the Kelvin equation

$$r_d^* = \frac{2\sigma v_l}{k_B T \ln S}. \quad (15)$$

The rate at which nuclei are born is e.g. given by the so-called classical nucleation theory [12]

$$J = \sqrt{\left(\frac{2m\sigma}{\pi\rho_l^2}\right)}N^2 \exp -\left(\frac{E^3}{2\ln^2 S}\right). \quad (16)$$

The liquid surface tension σ and the liquid density ρ_l are pure temperature functions as well as the energy parameter $E = 4\pi r_m^2\sigma/(1.5\,k_B T)$ with the molecular radius r_m based on the liquid density. The number density N of vapor molecules depends on temperature and vapor pressure by virtue of the equation of state. The saturation ratio S expresses the ratio of the vapor over the temperature dependent equilibrium vapor pressure. Thus a supersaturated state fixed by the variables T and p_v corresponds to a certain nucleation rate.

The idea of the experiment is to transfer a vapor diluted in a carrier into a supersaturated state for a short and sharply defined nucleation period. During this period of fixed state a finite number of nuclei per unit volume is born. The state after the nucleation period is kept supersaturated entailing condensational growth towards new phase equilibrium. Before this is

reached the state is brought back to undersaturation inducing reevaporation. The whole process is observed optically resulting in radius vs time plots.

Figure 1 outlines the principle experimental arrangement that realizes this idea. The employed gas-dynamic shock tube process is explained by a wave diagram and the pressure history at the observation station.

A basic shock tube consists of driver and driven section separated by a thin diaphragm. The diaphragm allows different pressures and gases in the two sections in the initial state of an experiment. In our case the driver contains carrier mixed with a small fraction of undersaturated vapor. The total pressure is close to atmospheric. The driven section holds pure carrier at a lower pressure. Everything is at room temperature. The experiment starts when the diaphragm is broken. A shock wave and an expansion wave form and travel into opposite directions. The shock compresses the driven gas while the expansion wave expands the carrier/vapor mixture. The gas is set into motion to the right. The expansion wave is delineated by two diverging lines called head and tail moving at the speed of sound relative to the gas. The gas is in the initial state '4' before the head and in the expanded state '3' behind the tail.

The pressure vs time plot to the left of Fig. 1 depicts the situation at the observation station close to the end wall. The initial pressure starts to drop when the head reaches the wall. The expansion wave is reflected leaving a constant state '6' behind the reflected tail which is the nucleation state. Because of the boundary condition of the wall the gas must be at rest in this state. The pressure p_6 can be tuned precisely by variation of the initial pressures. $S = 1$ marks where the vapor has passed saturation. Between this point and the nucleation state (≈ 1 ms) some undesired pre-nucleation may occur. Yet the rate is such an extreme function of S that prenucleation is of no practical importance [1].

The expansion wave expands the vapor/carrier mixture isentropically [1]. Therefore, with the ratio of specific heats γ of the mixture the temperature relates directly to the pressure, i.e.

$$\frac{T_6}{T_4} = \left(\frac{p_6}{p_4}\right)^{(\gamma-1)/\gamma}. \tag{17}$$

Since the initial mixing ratio remains constant throughout the expansion

$$\frac{p_6}{p_4} = \frac{p_{6v}}{p_{4v}}, \tag{18}$$

the supersaturation at nucleation is found from

$$S = \frac{p_{4v}}{p_4}\frac{p_6}{p_e(T_6)}. \tag{19}$$

The length of the nucleation period (≈ 0.3 ms) is controlled by a small recompression shock which follows the expansion tail. It stems from the tube constriction where the primary shock undergoes fractional reflection. The state of the growth period following nucleation is constant except for a small disturbance originating from interaction of the reflected expansion wave with the constriction.

After a growth period of typically 20–40 ms, far before droplet vapor equilibrium is reached, the vapor is undersaturated again by a strong shock wave. At first sight the primary shock reflected from the end wall of the driven section suggests itself for this purpose. Yet, it cannot be exploited because it is immediately neutralized by the following reflected expansion wave.

For this reason we introduce an artificial shock

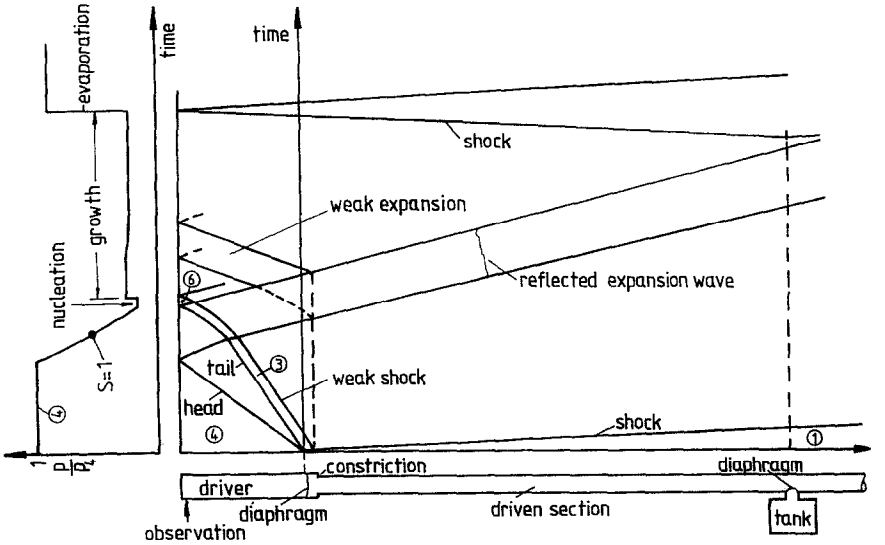

FIG. 1. Wave diagram of shock tube set-up with pressure history at the end wall of the driver section where droplet condensation and evaporation are observed.

generated by means of the tank attached to the side of the driven tube. In the initial state it is sealed from the driven tube by a diaphragm and filled with carrier gas. This diaphragm is broken after the primary shock and the reflected expansion have passed. At that instant the tank pressure exceeds the pressure of the driven gas so that shock waves build up moving into both tube directions. The one that goes upstream appears at the observation station as the reevaporation shock. The observation station is only a few millimeters away from the end wall so that incoming and reflected shock are hardly discernible. For the same reason the zero velocity condition of state 6 persists through the shock compression. Everything that goes downstream into a sufficiently long driven tube does not interfere with the observation station.

3.2. *The experimental set-up*

Figure 2 gives more details of the set-up. The diameter of the tube is 46 mm. The lengths are 1 m for the driver and 12 m for the driven section. The tank is placed 4 m away from the diaphragm station. The diaphragm between tank and tube is pierced by a (not shown) solenoid driven needle. The solenoid is controlled by a delay circuit triggered when the main diaphragm is punched out by a cutting ring (also not shown).

The vapor/carrier samples are prepared in the mixing tank by measuring partial pressures. First vapor evaporated from its bulk liquid phase in a bulb is led into the evacuated tank. After that carrier is added until a desired mixing ratio is established. A magnetic stirrer ensures perfect mixing. Prepared samples are transferred into the evacuated driver side.

The expansion pressure is measured by a calibrated piezo-quartz transducer. Partial and initial pressures are monitored by static pressure gauges. The initial temperature is checked by a PT 100. The signal is stored and processed in a transient recorder.

3.3. *Light scattering detection*

The growing and shrinking droplets are observed by a scattering technique based on Mie theory (Kerker [13]). An argon-ion laser (514.2 nm, 200 mW) is shone across the tube passing a stop of 1 mm diameter and two windows. Its intensity is monitored behind the second window by a power meter. Droplets present within the volume of the beam scatter in all directions. By means of 13 holes of 1 mm diameter and 70 mm length placed between glass wall and photomultiplier we select a scattering angle of $90 \pm 0.4°$ and 13 sensitive volumes along the beam of 8.67 mm^3 in total.

The photomultiplier converts light power, i.e. intensity times sensitive area, proportionally into voltage. The calibration factor was found to be $2(\pm 1)\ 10^8$ V W^{-1}. Mie theory provides scattered intensity normalized by incident intensity for a spherical droplet. When scattering angle and refractive index are fixed the intensity depends on the drop radius only. Figure 3 shows the relative scattered intensity multiplied by a factor accounting for the distance from the receiver. The refractive index is that of water and the scattering angle is normal to the beam and its direction of polarization reflecting the experimental situation. The numbered sequence of peaks identifies a corresponding sequence of radii. Accordingly, by reading experimental peaks as a function of time the radius is found as a function of time. The range before the first peak at 162 nm is not accessible by our experiment because here the intensity rapidly falls off to zero. The intensity behind the first peak stays within 2 orders of magnitude barely coverable by the photomultiplier.

Mie theory applies to a single droplet. When more than one droplet are present in the sensitive volume the scattered intensity is proportional to the number of scatterers supposing the scatterers are independent and monodispersed. Independent scattering can be supposed whenever the incident beam shows only weak attenuation. The second condition cannot be

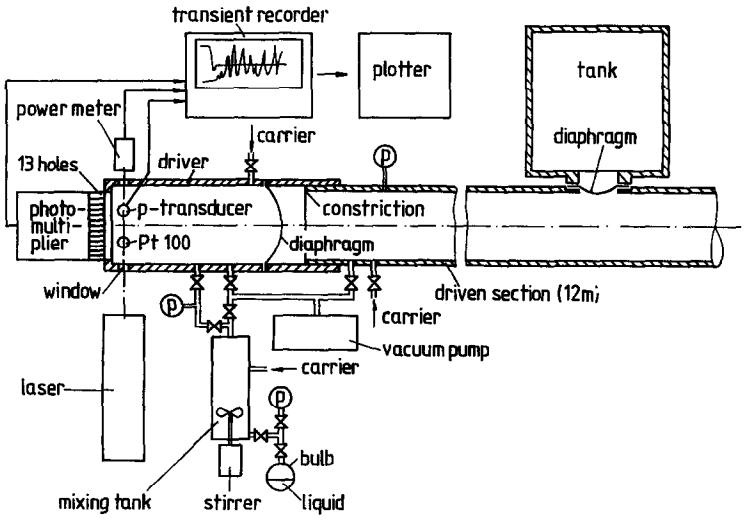

FIG. 2. Overview over shock tube set-up with vapor mixing station and scattering optics.

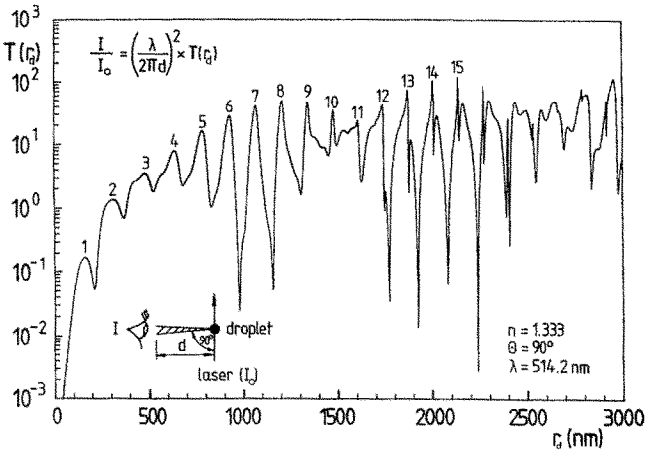

FIG. 3. Relative light intensity I/I_0 scattered from a single water droplet under given conditions according to Mie theory.

satisfied perfectly, however, due to the shortness of the nucleation period (≈ 0.3 ms) the size spectrum of nuclei born at the beginning and at the end of the period is kept rather narrow. Furthermore, since growth slows down with size according to the models, the size spectrum always shrinks. The existence of the size spectrum entails a slightly reduced signal amplitude of up to 10% at the first peak. The influence on the peak location or structure is marginal.

The combination of laser intensity, photomultiplier sensitivity, and scattering geometry brings about a minimum number of 50 droplets that need to be present at the first peak to produce a photomultiplier signal above noise level (5 mV). In terms of nucleation rate (divide 50 by sensitive volume and nucleation time) this is the order of 10^7 cm^{-3} s^{-1}. All our experiments are based on nucleation rates in the vicinity of 10^8 cm^{-3} s^{-1}. Droplet concentrations range from 10 to 1000 mm^{-3}.

4. RESULTS AND COMPARISON WITH MODEL

4.1. *Remarks on computation of growth and evaporation*

The change of radius vs time is computed from equations (11)–(14). This requires computation of dr/dt in time steps and integration. Computation starts at the critical radius r_d^* (equation (15)) of state 6. The number concentration of droplets is determined from the first peak. From step to step all needed quantities are recomputed according to sources referred to in the Appendix. The sticking coefficient α is taken to be unity.

The nucleation temperature follows from equation (17). The vapor pressure at nucleation p_{6v} and the saturation ratio S are computed from equations (18) and (19) with the measured total pressure p_6 and the mixing ratio p_{4v}/p_4. The pressures p_{4v} and p_{6v} are used as parameters in the $r(t)$ plots. Initial total pressure and temperature are close to atmospheric values.

The temperature change across the two shocks is obtained from the measured pressure ratio across the shock in conjunction with the shock relations [14]. The state parameters behind the shock T_∞, p_∞ and $p_{v\infty}$ appear in the $r(t)$ plots.

Vapor depletion by condensation or augmentation by evaporation has to be tracked accurately, i.e. the condensed mass needs to be known. This depends linearly on the number of droplets but to the third power on their size. Therefore, it is advisable to take into account the slight size distribution caused by the finite length of the nucleation period. To this end the nucleation period is divided into 10 intervals and a growth curve is computed for each interval. Then at any instant the mean radius of these curves is used.

The latent heat of condensation raises the ambient temperature of the vapor/carrier mixture. The heat of vaporization has the opposite effect. The condensed mass together with the heat capacity of the vapor/carrier mixture allows us to evaluate this effect for each time step.

4.2. *Measuring example*

Figure 4 gives a representative example of pressure and light signal as they are obtained from an experimental run. The pressure signal appears as predicted in Fig. 1. The peaks of the light signal are numbered corresponding to Fig. 3. We notice that the first peak occurs immediately after the nucleation period and that 14 peaks are counted before the strong shock appears. Now the light signal and the numbering is reversed since the droplets shrink. In this particular case the reversed signal is slightly stretched compared to the condensation signal meaning that condensation is slightly faster than evaporation. The time of occurrence of each peak is read off the time axis which starts at the nucleation period. That way the resulting radius vs time plots are obtained.

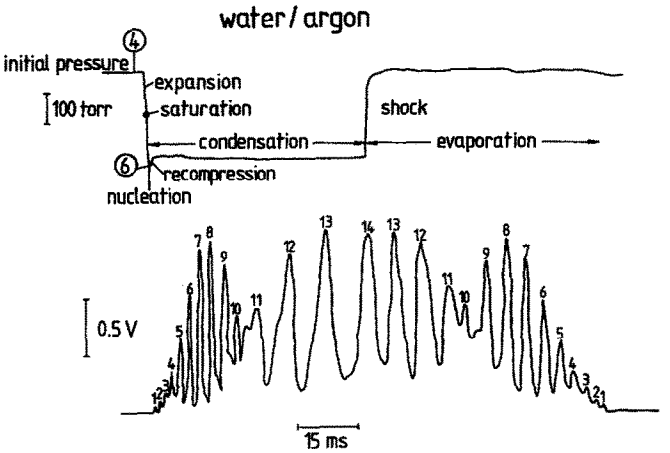

FIG. 4. Typical experimental run. Top: pressure signal. Bottom: corresponding light signal.

4.3. *Experimental range*

Experiments have been carried out with various vapors in various ranges. Here we present a selection of results on water, *n*-propanol, methanol and *n*-hexane carried in argon or air. Figure 5 delineates the test range of each of these vapors by two isentropes stretching between the initial state at room temperature and the nucleation state. The lines connecting the circles are the equilibrium vapor pressure curves. The lines between the dots represent nucleation states (10^8 cm^{-3} s^{-1}) where growth starts. Dividing any pressure on these lines at any temperature by the corresponding equilibrium pressure $p_e(T)$ yields the supersaturation at nucleation. The numbers indicate supersaturations at the dots. The dashed line samples a full experimental cycle. After isentropic expansion between a and b nucleation takes place in b terminated by the small recompression shock (bc). The vapor is depleted between c and d by condensation. The evaporation shock transfers the vapor back into the undersaturated regime from d to e where evaporation ensues. The highest evaporation temperature reached in this work is about 400 K.

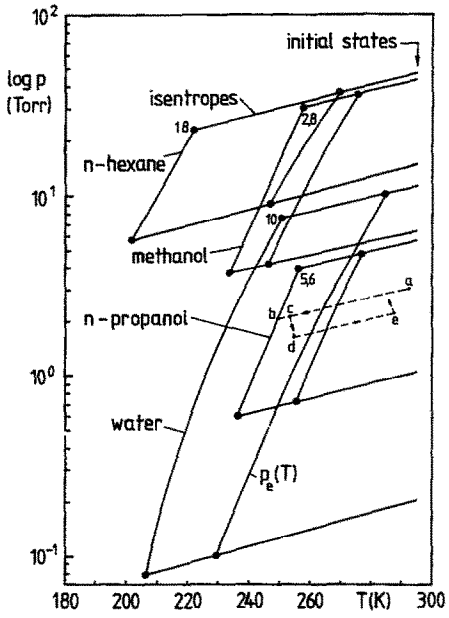

FIG. 5. Overview of investigated vapors and their ranges. Shown are initial states, upper and lower expansion isentropes, equilibrium vapor pressures $p_e(T)$ (lines between circles) and nucleation states (lines between dots) for nucleation rates of about 10^8 cm^{-3} s^{-1}. The numbers indicate the supersaturation at the upper dot. The dashed line outlines an experimental cycle. ab: isentropic expansion with nucleation in b; bc: recompression shock; cd: growth; de: evaporation shock; from e: evaporation.

4.4. *Results*

Figure 6 shows growth of *n*-propanol droplets in argon. The droplet radius is plotted in nm (10^{-9} m) vs time in ms (10^{-3} s). Each data point reflects a peak of the Mie signal. The curves represent the model calculations. The critical radius being of the order of a nm is not discernible on the scale of this plot. The slight irregularities of the curves shape stem from

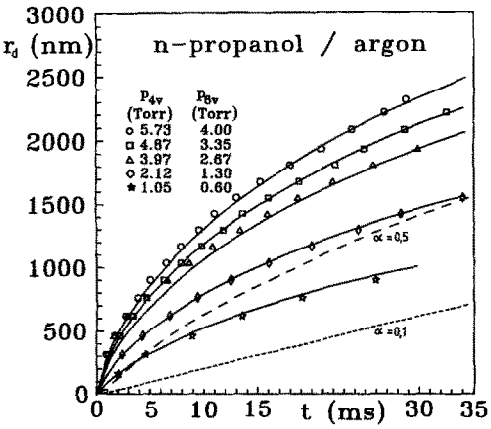

FIG. 6. Growth of *n*-propanol droplets in argon. Points: experimental results with initial p_{4v} and nucleation vapor pressure p_{6v}. Dashed curves: model computed for sticking coefficients smaller than unity corresponding to fourth curve from top.

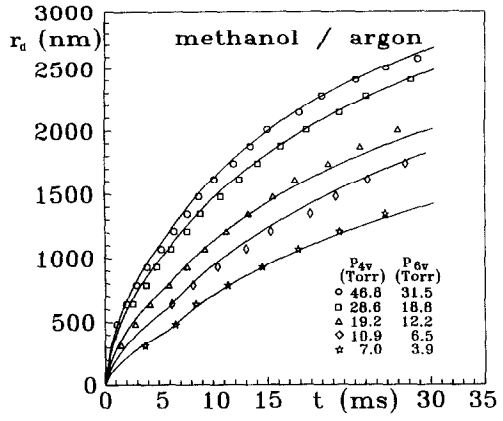

FIG. 7. Growth of methanol droplets in argon like Fig. 6.

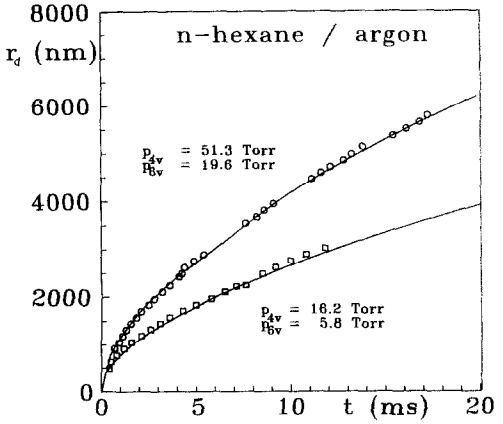

FIG. 9. Growth of *n*-hexane droplets in argon like Fig. 6.

pressure disturbances. We see that the model agrees very well with the experimental data. The two dashed curves belong to the fourth curve from top. They give the full model for sticking coefficients of $\alpha = 0.5$ and $\alpha = 0.1$. This example clearly substantiates the assumption of a sticking coefficient of unity.

Figures 7 and 8 demonstrate the influence of the carrier (argon or air) on the growth of methanol droplets. The heat conductivity of air is greater than that of argon. This makes growth in air faster than in argon. The two plots show that this effect of the carrier gas is perfectly covered by the model. It must be noted at this point that methanol molecules associate in the prenucleation state. The heat of associating molecules has to be regarded when determining the state of nucleation. This problem has been dealt with earlier [12].

Figure 9 presents *n*-hexane, a substance with a comparatively small latent heat. A reduced latent heat allows more mass to condense per unit time, i.e. an increased growth rate. We see that *n*-hexane in fact grows to much greater sizes than the other substances on the same time scale. The model covers this extreme case with unyielding accuracy. Since growth is so fast the peaks draw closer and in places identification becomes difficult. This is why the upper data line exhibits gaps.

Figure 10 presents evaporation curves for water droplets in argon. The three evaporation curves are produced by variation of the evaporation shock strength while repeating the same condensation process. They were meant to start at the same radius. Difficulties in triggering the arrival time of the shock at the observation station are responsible for this blemish. The three entries with subscript ∞ determine the state after the shock, i.e. at the beginning of evaporation. The two data points on the time axis ($r_d = 0$) do not represent peaks. They were taken at the lowest detectable light level corresponding to less than 50 nm where total evaporation has practically been reached.

The good agreement between model and data provokes the question for the limits of the model and the experiment itself.

The experimental limit is the Mie signal. It loses clarity with growing shock strength. This is not only because the peaks draw closer. It is also because residual size distributions broaden with increasing

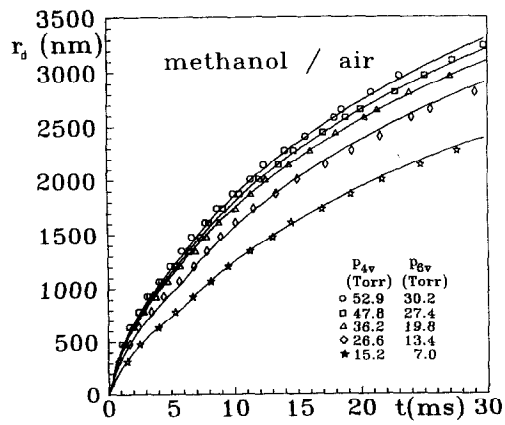

FIG. 8. Growth of methanol droplets in air like Fig. 6.

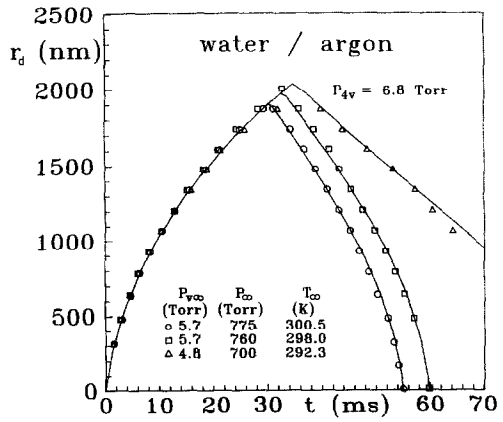

FIG. 10. Growth and evaporation of water droplets in argon. There is one growth curve for three evaporation curves distinguished by the vapor pressure $p_{v\infty}$, the total pressure p_∞ and the temperature T_∞ at the beginning of evaporation, i.e. after the shock.

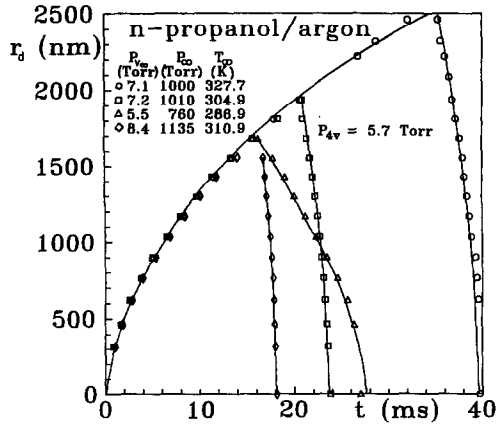

FIG. 11. Growth and evaporation of *n*-propanol droplets in argon like Fig. 10.

evaporation rates. We studied high evaporation rates in the case of *n*-propanol droplets in argon and found identifiable Mie signals for evaporation temperatures up to 400 K. The results are displayed in Fig. 11. A fourfold repeated growth curve branches into four evaporation curves. The curve with the smallest slope resembles those of the previous figure. The others are much steeper reaching evaporation rates as high as 0.5 μm ms^{-1}. Still, agreement with theory is retained. One of the curves (T_{∞} = 327.7 K) reappears in Fig. 12 on a stretched time scale together with other curves corresponding to highly compressed, hardly readable Mie signals. At the same time substantial deviation from the model occurs. This is, however, not unexpected because the deviation from equilibrium becomes too large with temperature differences reaching 100 K.

5. CONCLUSION

We have extended a gasdynamic shock tube method, originally developed to measure homogeneous nucleation rates [1], to the study of growth and evaporation of droplets in carrier gases. Homogeneous nucleation is now merely exploited as a droplet generation mechanism. It provides monodispersed droplet suspensions without interference of walls or foreign aerosols, a perfect starting-point for growth and evaporation studies. The combination of Mie light scattering as a droplet detection method with shock tube gas dynamics and homogeneous nucleation has proved to be successful. It has produced a great deal of radius vs time results in a wide Knudsen number range for substances with different physical properties.

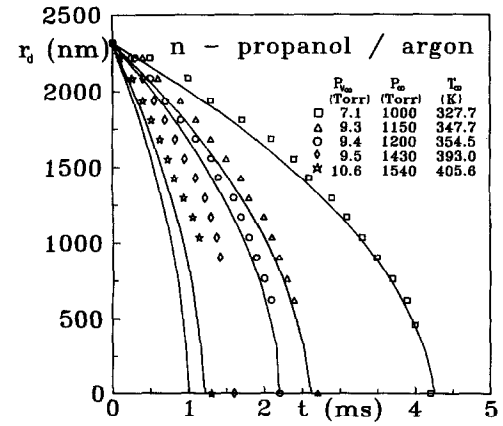

FIG. 12. Very fast evaporation of *n*-propanol in argon. Condensation curve not shown.

Throughout the experimental range the results agree with a growth and evaporation model as revised by Young [11] provided condensation and evaporation coefficients of unity. This should not be interpreted as a general result for these coefficients. According to the broad scatter of literature values they may be strongly dependent on the experimental conditions. The application of the model has to include a continuous updating of the ambient conditions on basis of a heat and mass balance. The limits of the model show at high evaporation rates of the order 1 μm ms^{-1} coinciding with experimental limits of the optical detection.

In conclusion we have contributed systematic measurements to the droplet growth and evaporation problem which has seen a great deal of theoretical work in contrast to few experimental investigations. The good agreement with theory provides a sound basis for further work with e.g. higher number concentrations, moving or polydispersed droplets.

Acknowledgement—This work was supported by grant Me 484/16 of Deutsche Forschungsgemeinschaft (DFG).

REFERENCES

1. F. Peters and B. Paikert, Nucleation and growth rates of homogeneously condensing water vapor in argon from shock tube experiments, *Exp. Fluids* **7**, 521–530 (1989).
2. M. A. Vietti and J. L. Fastook, Water droplet growth in a carbon dioxide atmosphere: A case for small sticking coefficient, *J. Chem. Phys.* **65**(1), 174–178 (1976).
3. P. E. Wagner, Aerosol growth by condensation. In *Aerosol Microphysics* (Edited by W. H. Marlow), Vol. II, Chap. 5, pp. 129–178. Springer, Berlin (1982).
4. P. E. Wagner, The interdependence of droplet growth and concentration. II. Experimental test of droplet growth theory, *J. Colloid Interface Sci.* **53**(3), 439–446 (1975).
5. D. E. Hagen, J. Schmitt, M. Trueblood and J. Carstens, Condensation coefficient measurement for water in the UMR cloud simulation chamber, *Am. Meteorological Soc.* 803–816 (1989).
6. P. Roth and R. Fischer, An experimental shock wave study of aerosol droplet evaporation in the transition regime, *Phys. Fluids* **28**(6), 1665–1672 (1985).
7. H. W. J. Goosens, J. W. Cleijne, H. J. Smolders and M. E. H. van Dongen, Shock wave induced evaporation of water droplets in a gas-droplet mixture, *Exp. Fluids* **6**, 561–568 (1988).
8. G. Gyarmathy, The spherical droplet in gaseous carrier streams: Review and synthesis. In *Handbook of Chemistry and Physics* (62nd Edn), *Multiphase Science and Technology*, Vol. 1, pp. 99–279. McGraw-Hill, New York (1982).

9. M. Mozurkewich, Aerosol growth and the condensation coefficient for water: A review, *Aerosol Sci. Technol.* **5**, 223–236 (1986).
10. J. C. Barret and C. F. Clement, Growth rates for liquid drops, *J. Aerosol Sci.* **19**(2), 223–244 (1988).
11. J. B. Young, The condensation and evaporation of liquid droplets at arbitrary Knudsen number in the presence of an inert gas, *Int. J. Heat Mass Transfer* **36**, 2941–2956 (1993).
12. F. Peters and B. Paikert, Experimental results on the rate of nucleation in supersaturated *n*-propanol, ethanol, and methanol vapors, *J. Chem. Phys.* **91**(9), 5672–5678 (1989).
13. M. Kerker, *The Scattering of Light and other Electromagnetic Radiation*. Academic Press, New York (1969).
14. H. Liepmann and A. Roshko, *Elements of Gasdynamics*. Wiley, New York (1957).
15. *CRC Handbook of Chemistry and Physics* (61st Edn) (Edited by R. G. Weast). CRC Press, Boca Raton (1980).
16. A. H. P. Skelland, *Diffusional Mass Transfer*. Wiley, New York (1974).
17. J. O. Hirschfelder, C. F. Curtiss and R. B. Bird, *Molecular Theory of Gases and Liquids*. Wiley, New York (1954).
18. Landolt-Börnstein, *Zahlenwerte und Funktionen*, Vol. 4(4b). Springer, Berlin (1972).
19. H. R. Pruppacher and J. D. Klett, *Microphysics of Clouds and Precipitation*. Reidel, Holland (1980).
20. R. Strey and T. Schmeling, Surface tension measurements for the *n*-alcohols in the temperature range from −40°C to +40°C, *Ber. Bunsenges. Phys. Chem.* **87**, 324–327 (1983).
21. T. Schmeling and R. Strey, Equilibrium vapor pressure measurement for the *n*-alcohols in the temperature range from −30°C to +30°C, *Ber. Bunsenges. Phys. Chem.* **87**, 871–874 (1983).
22. J. L. Katz and B. J. Ostermier, Diffusion cloud-chamber investigation of homogeneous nucleation, *J. Chem. Phys.* **47**, 478–487 (1967).
23. D. Sonntag and D. Heinze, Sättigungsdampfdruck und Sättigungsdampfdichtetafeln für Wasser und Eis. VEB, Leipzig (1982).
24. S. Z. Mikhail and W. R. Kimel, Densities and viscosities of 1-propanol–water mixtures, *J. Chem. Engng Data* **8**, 323–328 (1963).

APPENDIX. PHYSICAL PROPERTIES

(Note: T in K and T_c in °C everywhere.)

Diffusion coefficient D

From ref. [17]; the necessary molar weights and the molecular potential energy parameters s and ε/k_B are listed above.

Heat conductivity k from ref. [18]

$k = (1.8981 + 0.051\ T)/1000$ for argon in W m^{-1} K^{-1}

$k = 4.186\ (5.69 + 0.017\ T_c)/1000$ for air in W m^{-1} K^{-1}.

Surface tension in N m^{-1}

$\sigma = 0.0761 - 1.55\ 10^{-4}\ T_c$ water

$\sigma = (24.23 - 0.09254\ T_c)/1000$ methanol

$\sigma = (25.28 - 0.08394\ T_c)/1000$ *n*-propanol

$\sigma = (20.46 - 0.104\ T_c)/1000$ *n*-hexane.

Equilibrium vapor pressure in Torr

$p_e = 0.0075 \exp(21.125 - 2.7246 \times 10^{-2}\ T + 1.6853 \times 10^{-5}\ T^2 + 2.4576 \ln(T) - 6094.4642/T)$ water

$p_e = \exp(87.4776 - 7543.0896/T - 10.06 \ln(T))$ methanol

$p_e = \exp(150.248 - 11286.4904/T - 19.19 \ln(T))$ *n*-propanol

$\log p_e = 6.8778 - 1171.53/(T - 48.78)$ *n*-hexane.

Liquid density in kg m^{-3}

$\rho_l = 999.84 + 0.086\ T_c - 0.0108\ T_c^2$ water

$\rho_l = 801 - 0.9253\ T_c - 4.1 \times 10^{-4}\ T_c^2$ methanol

$\rho_l = 799.5 - 0.82\ (T_c - 25)$ *n*-propanol

$\rho_l = 677.02 - 0.8883\ T_c - 4.765 \times 10^{-4}\ T_c^2$ *n*-hexane.

Sources for data on surface tension, equilibrium vapor pressure and liquid density: [19–24].

The latent heat is inferred from the Clausius–Clapeyron equation.

	water	meth.	*n*-prop.	*n*-hex.	argon	air	unit	ref.
M	18.02	32.04	60.11	86.18	39.95	28.96	g mol^{-1}	15
c_p	1858	1317	1455	1384	519	1004	N m mol^{-1} K^{-1}	15
n	1.333	1.329	1.385	1.375				15
γ	1.330	1.246	1.105	1.075	1.667	1.4		15
s	2.641	3.626	4.549	5.949	3.542	3.711	10^{-10} m	16
ε/k_B	809.1	481.8	576.7	399.3	93.3	78.6	K	16